

Energy & Environmental Science

Accepted Manuscript



This is an *Accepted Manuscript*, which has been through the Royal Society of Chemistry peer review process and has been accepted for publication.

Accepted Manuscripts are published online shortly after acceptance, before technical editing, formatting and proof reading. Using this free service, authors can make their results available to the community, in citable form, before we publish the edited article. We will replace this *Accepted Manuscript* with the edited and formatted *Advance Article* as soon as it is available.

You can find more information about *Accepted Manuscripts* in the [Information for Authors](#).

Please note that technical editing may introduce minor changes to the text and/or graphics, which may alter content. The journal's standard [Terms & Conditions](#) and the [Ethical guidelines](#) still apply. In no event shall the Royal Society of Chemistry be held responsible for any errors or omissions in this *Accepted Manuscript* or any consequences arising from the use of any information it contains.

Highly Efficient Planar Perovskite Solar Cells through Band Alignment Engineering

Juan Pablo Correa Baena,^{1*} Ludmilla Steier,² Wolfgang Tress,^{2,3} Michael Saliba,³ Stefanie Neutzner,⁴ Taisuke Matsui,⁵ Fabrizio Giordano,² T. Jesper Jacobsson,¹ Ajay Ram Srimath Kandada,⁴ Shaik M. Zakeeruddin,^{1,2} Annamaria Petrozza,⁴ Antonio Abate,² Mohammad Khaja Nazeeruddin,³ Michael Grätzel,² and Anders Hagfeldt^{1*}

¹Laboratory for Photomolecular Science, Institute of Chemical Sciences and Engineering, École Polytechnique Fédérale de Lausanne, CH-1015-Lausanne, Switzerland.

²Laboratory for Photonics and Interfaces, Institute of Chemical Sciences and Engineering, École Polytechnique Fédérale de Lausanne, CH-1015-Lausanne, Switzerland.

³Group for Molecular Engineering of Functional Materials, Institute of Chemical Sciences and Engineering, École Polytechnique Fédérale de Lausanne, CH-1015-Lausanne, Switzerland

⁴Center for Nano Science and Technology@Polimi, Istituto Italiano di Tecnologia, via Pascoli 70/3 20133 Milano, Italy

⁵Advanced Research Division, Panasonic Corporation, 1006, (Oaza Kadoma), Kadoma City, Osaka 571-8501, Japan.

*Corresponding authors: AH anders.hagfeldt@epfl.ch; JPCB juan.correa@epfl.ch.

JPCB and LS contributed equally to this work.

Keywords: Perovskite solar cell, hysteresis, electron selective layers, photovoltaics, SnO₂, TiO₂.

Abstract

The simplification of perovskite solar cells (PSCs), by replacing the mesoporous electron selective layer (ESL) with a planar one, is advantageous for large-scale manufacturing. PSCs with a planar TiO₂ ESL have been demonstrated, but these exhibit unstabilized power conversion efficiencies (PCEs). Herein we show that planar PSCs using TiO₂ are inherently limited due to a conduction band misalignment and demonstrate, with a variety of characterization techniques, for the first time that SnO₂ achieves a barrier-free energetic configuration, obtaining almost hysteresis-free PCEs of over 18% with record high voltages up to 1.19 V.

Introduction

Solution processed, hybrid organic-inorganic perovskite materials were studied by Mitzi et al. in the 1990s and were recognized as excellent semiconducting materials.¹ It was not, however, until Miyasaka and coworkers pioneered the work on dye-sensitized solar cell applications in 2009, that the material started to be recognized by the photovoltaic community.² Since then, a myriad of works has been published exploring different device configurations. The currently highest reported PCE value of over 20% was achieved using a thin layer of mesoporous TiO₂.³ In this architecture, the perovskite material, infiltrates a mesoporous TiO₂ layer which is sandwiched between a hole transporting layer (HTL, typically doped 2,2',7,7'-tetrakis(*N,N'*-di-*p*-methoxyphenylamine)-9,9'-spirobifluorene (Spiro-OMeTAD) or polytertiary arylamine (PTAA)) and an electron selective layer (ESL, typically TiO₂).

From the earlier works, it was realized that the perovskite absorber material transports both holes and electrons.⁴⁻⁶ Naturally, this led towards the investigation of a thin film perovskite configuration with only a compact TiO₂ as the ESL.⁷ However, this device architecture shows pronounced hysteresis of the current voltage (J-V) curve,⁸⁻¹⁰ especially for fast voltage sweeps and to our knowledge no PCE of over 18% in this architecture has been reported without hysteresis and stabilized power output. Xing et al. showed that planar devices using PCBM as the ESL and methyl ammonium lead iodide (MAPbI₃) as the absorbing and transporting material, had a much improved J-V hysteretic behaviour when compared to TiO₂ ESL, which they linked to the improved interfacial charge transfer. Wojciechowski and co-workers showed that modifying the TiO₂ surface with fullerene derivatives can work towards high efficiency PSCs.⁸ Recent

works have shown the potential of SnO₂-based ESLs,¹¹⁻¹⁴ but so far these devices have not shown high efficiency without hysteretic behaviour.

Using a low temperature atomic layer deposition (ALD) process to fabricate SnO₂ ESLs, we demonstrate that planar PSCs can achieve almost hysteresis-free of above 18% with voltages exceeding 1.19 V. We show that this is not the case for the planar TiO₂. We choose SnO₂ considering the favourable alignment of the conduction bands of the perovskite materials and the ESL and show an energy mismatch in the case of TiO₂. Thus, using SnO₂, which has a deeper conduction band, enables us to fabricate planar devices with high efficiencies, long term air stability and improved hysteretic behaviour, while keeping the processing at low temperatures (< 120 °C), which is key for process upscaling and high efficiency tandem devices.¹⁵

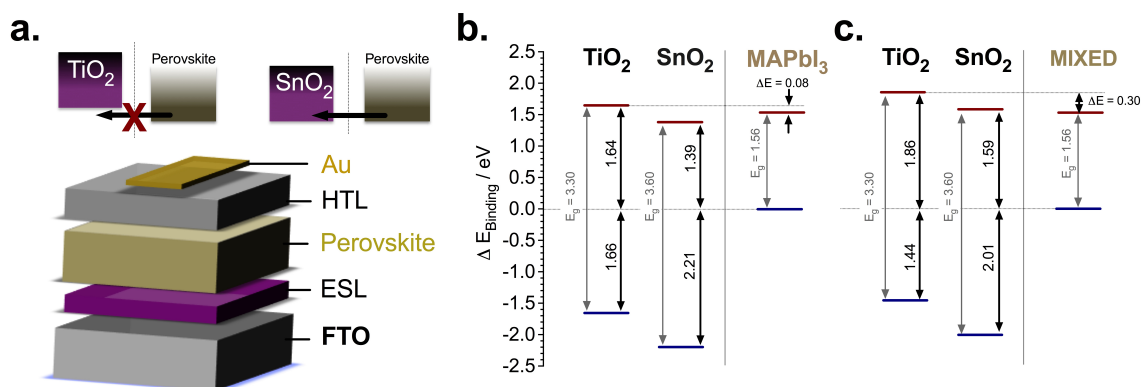


Figure 1. Energy level diagrams and electron injection characteristics of SnO₂ and TiO₂-based planar PSCs. **a**, Schematic energy level diagram of the perovskite films and the electron selective layers, TiO₂ and SnO₂ for **b**, MAPbI₃ and **c**, (FAPbI₃)_{0.85}(MAPbBr₃)_{0.15}, labeled as ‘mixed’.

Results and Discussion

In Figure 1a, we illustrate how electron injection is energetically hindered when the bands are mismatched. This is accompanied by a schematic of the planar device architecture of a typical glass/FTO/compact metal oxide/perovskite/hole transporter/gold stack. We analyse the band structure further using ultraviolet photoelectron spectroscopy (UPS) for two different perovskite materials (MAPbI₃ and mixed halide/cation, i.e. (FAPbI₃)_{0.85}(MAPbBr₃)_{0.15}, referred to as mixed perovskite throughout the text) atop the TiO₂ and SnO₂ as shown in Figure 1b and c as derived from Supplementary Figures S1 and S2, respectively. The ionization energy (IE), e.i. valence band position, measurements of the SnO₂ and TiO₂ were performed for the UV ozone-treated samples atop FTO, thus obtaining the valence band information for both substrates. It has been shown that the valence band position of the perovskite material measured by UPS has variations with respect to the substrate where they are deposited.¹⁶ Thus, we performed our measurements on perovskite films deposited on both SnO₂ and TiO₂ yielding IE differences of above 0.1 eV. We calculated the band diagram of the different components using the perovskite materials' valence bands as our reference. The construction of the band diagram, including bandgap estimation for the perovskite materials (thickness of ca. 400 nm), is described in the Supplementary Figure S1-3. We found that for both perovskite materials there is a conduction band misalignment with TiO₂ ESLs, in stark contrast to SnO₂ where we have no such misalignment. The band diagram in Figure 1b, shows that the conduction band of MAPbI₃ is ~80 meV below than that of TiO₂ and about 170 meV above that of SnO₂. This inhibits electron extraction by the TiO₂ and facilitates it using SnO₂. Similarly, the conduction band of the mixed perovskite is 300 meV below compared to TiO₂ and only 30 meV below compared to SnO₂. Consequently,

this band misalignment with TiO_2 may cause undesirable consequences such as accumulation of photogenerated charges, which could hamper the device performance.

It is important to note that the UPS measurements were carried out on perovskite films as thick as 400 nm. Since UPS is a surface measurement (measuring roughly the conditions in the first 10 nm), it is therefore a simplified picture our device energetics. Guerrero et al. have shown that the energetics throughout the perovskite film can be different and that bandbending can be induced when employing thick films.¹⁷ In addition, work by some of us has also shown that ion migration is induced in the perovskite material,¹⁸ which further complicates the energetic model in the device. Indeed, these two factors play a major role in the electronic configuration of the device and it is something that will be further investigated more in depth in future studies. However, with these measurements we elucidate that there is an intrinsic difference between the two ESL, which lead to understand that there is an energetic barrier at the TiO_2 , but not at the SnO_2 /Perovskite interface.

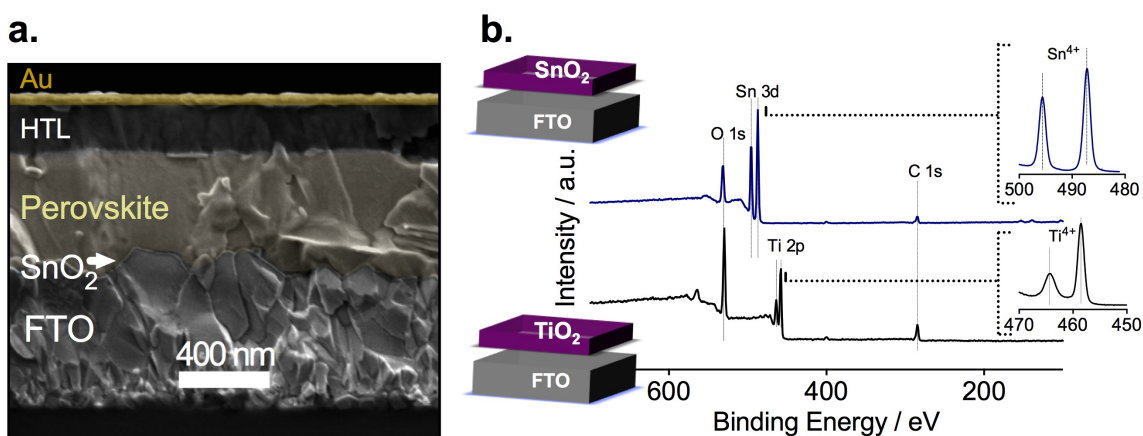


Figure 2. Photovoltaic device architecture and elemental composition of the electron selective layers (ESLs). **a**, Cross-sectional scanning electron micrograph of a typical

layered photovoltaic device composed of FTO, SnO₂ as the electron selective layer (ESL), the perovskite film, a hole transporting layer (HTL, Spiro MeOTAD), and a gold top electrode. **b**, X-ray photoelectron spectroscopy of TiO₂ and SnO₂ thin layers used as ESLs.

To further investigate this phenomenon, we prepared planar devices of typical stack architecture: glass/FTO/ESL/perovskite/HTL/gold contact as seen in the cross-sectional scanning electron microscopy (SEM) image in Figure 2a. We deposited a 15 nm thick ESL of SnO₂, TiO₂ or Nb₂O₅ by ALD. The mixed perovskite layer, (FAPbI₃)_{0.85}(MAPbBr₃)_{0.15}, was spin-coated on the electrode using a similar composition as reported by Jeon et al.¹⁹ A doped spiro-MeOTAD was spin-coated as the HTL and, finally, the gold top electrode was deposited by thermal evaporation.

Figure 2b shows the X-ray photoelectron spectroscopy (XPS) of the 15 nm thick TiO₂ and SnO₂ layers. For TiO₂, no peaks other than oxygen O 1s at 528 eV, titanium Ti 2p at 458.5 eV and Ti 2p_{1/2} 464.2 eV were detected confirming the deposition of TiO₂ without traces of cross contamination.²⁰ We detect no signal from the underlying FTO indicating conformal and pinhole-free TiO₂ coverage, which we further confirm by SEM (see Supplementary Figure S4a). Similarly, we confirm the formation of pure SnO₂ observing the oxygen peak O 1s at 530.9 eV and Sn⁴⁺ peaks at 495.6 eV as well as at 487.2 eV. The top-view SEM image also indicates a pinhole-free deposition of SnO₂ (see Supplementary Figure S4b).

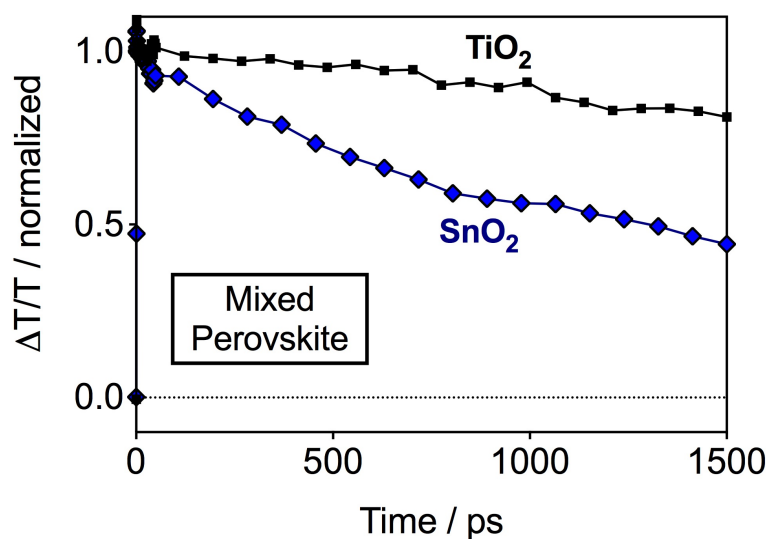


Figure 3. Transient absorption measurements of SnO₂ and TiO₂-based planar PSCs. Dynamics of the photo-bleaching bands for photo-excited perovskite measured on a typical working device employing the mixed perovskite (FAPbI₃)_{0.85}(MAPbBr₃)_{0.15} and SnO₂ or TiO₂ as the ESL. The device is held at short circuit condition during the measurement. The probe wavelength is $\lambda = 750$ nm.

In order to further understand the results by UPS in a device configuration we performed femtosecond transient absorption (TA) measurements. With this we intended to understand electron injection dynamics from the perovskite into the ESLs, and therefore, indirectly probe whether an energetic barrier exists for TiO₂ or SnO₂. The measurements were performed on devices with SnO₂ and TiO₂ and the mixed perovskite under short circuit condition, wherein the charge injection can be resolved in time. In Figure 3, we show the TA dynamics taken at a probe wavelength of 750 nm - the peak of the photobleach (PB) of the perovskite. The PB band, spectrally located at the onset of the absorption spectrum of the semiconductor (Supplementary Figure S3), corresponds to the

photo-induced transparency in the material due to the presence of electrons and holes in the bottom and top of the conduction and valence bands, respectively.¹⁷ Hence, the magnitude of this feature is correlated to the photo-induced carrier population and every effect changing the initial population, like electron/hole injection results in its quenching. We observe a PB decay in the nanosecond timescale for both TiO₂ and SnO₂-based devices. However, while in the TiO₂-based device the dynamic does not strongly differ from the one probed from the pristine perovskite deposited on bare glass,²¹ in the case of SnO₂ the decay is much faster. In fact, about 60% of the population is gone in about 1.5 ns. As both devices embody the same hole extracting layer, we conclude that the striking difference observed can be considered as the signature of different electron injection dynamics. This strongly supports our hypothesis of better electron extraction in pristine SnO₂ when compared to TiO₂-based devices, due to favorable energetic alignment.

We note that the poor charge extraction in the TiO₂ based device may appear surprising. However, it must be considered that, in thin film PSCs in presence of planar TiO₂ as electron extracting layer, solar cells generally show J_{SC} comparable to those using a mesoporous TiO₂ layer only when the device is pre-polarized.^{8, 9, 22-24} Indeed, some of us have recently demonstrated that the PB dynamics becomes faster when it is measured just after keeping the TiO₂-based device at 1 V for a few seconds, suggesting that the electron transfer is suddenly activated.²³ This indicates that upon polarization, the TiO₂/perovskite interface is modified and such modification is needed to allow for an efficient charge transfer as also predicted by De Angelis et al.²⁵

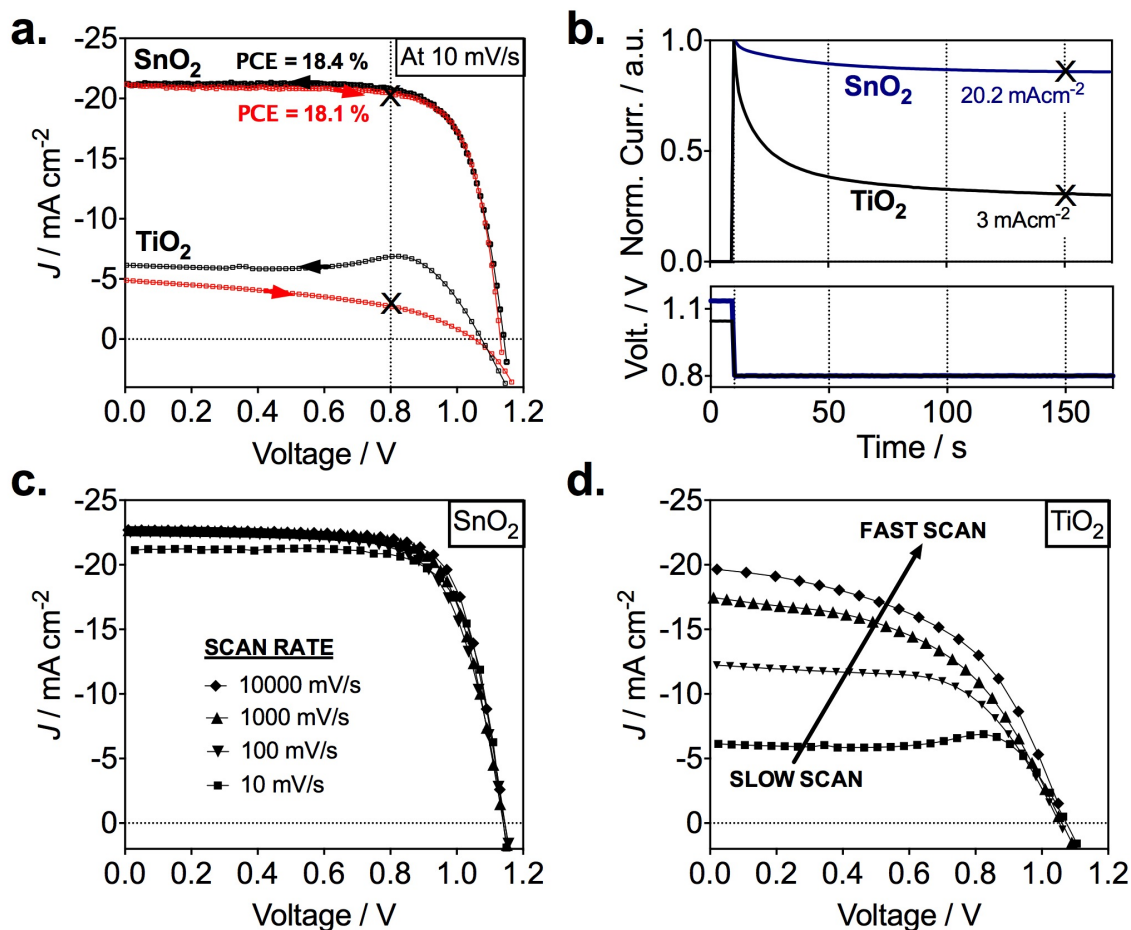


Figure 4. Photovoltaic characteristics of planar perovskite devices based on SnO_2 and TiO_2 ESL. **a**, Current-voltage properties of TiO_2 and SnO_2 -based planar mixed halide/cation perovskite devices. Black arrows indicate backward scan from V_{oc} to J_{sc} and red arrows indicate the reversed scan. **b**, Normalized transient photocurrents measured from V_{oc} to maximum power point voltage for both planar systems. **c**, Scan rate effects on J-V characteristics of SnO_2 and **d**, TiO_2 -based devices. We note that devices showed best performance when measured after 1 week of preparation.

We investigated the different electronic properties of devices with TiO_2 or SnO_2 ESLs by analyzing the current density-voltage curves based on the mixed perovskite. In Figure 4a,

we observe a representative SnO₂ device with high performance and low hysteresis between the backward and forward scan (Table 1). This is indicative of good charge collection independent of voltage. In stark contrast, a representative TiO₂-based device shows strong hysteresis and low current densities (<5 mA cm⁻²). This difference can also be seen in Figure 4b where we show transient photocurrents recorded at 0.8 V resembling closely operating device conditions at maximum power point. After ~50 s, we observe a steady photocurrent when switching from open circuit to 0.8 V. After switching from open circuit to 0.8 V, the current for the TiO₂ device drops by 70% from 10 to a stabilized 3 mA cm⁻², whereas that for the SnO₂ drops by only 10% from 23 to a stabilized 20.2 mA cm⁻². The stabilized current is in good agreement with the current seen in the J-V curve at 0.8 V, which is found to be 20.7 mA cm⁻² (Figure 4a). In addition, SnO₂-based devices showed good long-term stability; unencapsulated devices stored in dry air were measured for over 30 days with no significant PCE variability (Supplementary Figure S5). Small variations were found for 12 devices made in different batches with an average PCE of 16.7% (Supplementary Figure S6). Integrating the external quantum efficiency (EQE) yielded a J_{SC} of 18 mA cm⁻² (Figure S7a), which is in very good agreement with the measured J_{SC} in Figure S7b.

Table 1. Solar cell performance parameters for the mixed perovskite and SnO₂ device for backward and forward scans at a scan rate of 10 mV/s: short circuit photocurrent (J_{sc}), power conversion efficiency (PCE), open circuit voltage (V_{oc}), fill factor (FF) as extracted from the data in Figure 3a.

ESL	Scan	J_{sc}	V_{oc}	FF	PCE	Light intensity
-----	------	----------	----------	----	-----	-----------------

	direction	(mA cm ⁻²)	(V)	(%)	(mW cm ⁻²)
SnO₂	backward	21.3	1.14	0.74	18.4
	forward	21.2	1.13	0.75	18.1

We note that for both TiO₂ and SnO₂, we observe open circuit voltages of around 1.14 V, which are close or even exceeds most devices prepared with mesoporous interlayers. Additionally, some of our SnO₂ devices yielded stabilized voltages of over 1.19 V (Supplementary Figure S7c) approaching the thermodynamic maximum V_{oc} of approx. 1.32 V.²⁶ This suggests exceptionally good charge selectivity and a low degree of charge recombination in our planar perovskite/SnO₂ devices.

To understand the reason for the reduced photocurrent for the TiO₂ based device, we performed current-voltage scans at varied voltage sweep rates. These are shown in Figure 4c and d, where only the backward scan is plotted which is obtained after the device was preconditioned at 1.2 V for 10 s. For the SnO₂ device there is only a slight increase of the photocurrent when increasing the rate from 10 to 10 000 mV/s. Slightly enhanced sweep rates allow to collect almost all the photogenerated charges reaching a maximum J_{SC} density of 23 mA cm⁻². The dependence on scan rate is much more pronounced for the TiO₂-based device showing high current densities of ca. 20 mA cm⁻² for the scan at 10 V/s with a massive drop to about 5 mA cm⁻² when scanned at 10 mV/s. This implies a low charge collection efficiency in the planar perovskite/TiO₂ device at slow scan rates, though light absorption and photocurrent generation in the perovskite material is the same as for the perovskite/SnO₂ configuration. The results are also in good agreement with the transient photocurrent in Figure 4b, the electron injection characteristics in Figure 3 and

our proposed band alignment measured by UPS in Figure 1, clearly indicating a barrier free charge transport across the perovskite/SnO₂ in contrast to the perovskite/TiO₂ interface. We investigated devices with ALD Nb₂O₅ as the ESL (Supplementary Figure S8) which has a similar conduction band position as TiO₂.²⁷ With this, we can crosscheck if the energy level alignment is indeed critical for high hysteresis and can exclude that other properties of the SnO₂ or TiO₂ are responsible for the above results. Very similar to TiO₂, the Nb₂O₅-based devices exhibited large hysteresis behavior and very low photocurrent densities (Supplementary Figure S8). Several independent studies have shown similar or even more pronounced trends irrespective of TiO₂ deposition method. Spin-coating,^{8, 9, 23, 28-30} Sputtering^{30, 31} and spray pyrolysis³² of TiO₂ have all been demonstrated to yield highly hysteretic J-V curves in planar PSCs.

To further confirm what is found in the literature and show that our results are not unique to the ALD technique, we prepared TiO₂ by spray pyrolysis and found that the J-V curves exhibit strong hysteretic behavior (Supplementary Figure S9). In this case, the forward scan shows an s-shaped J-V curve indicative of unstabilized power output.³³ However, the devices using spray-pyrolysed TiO₂ showed an increase in the J_{sc} in the backward scan when compared to ALD TiO₂. In order to understand the difference between these two layers, we investigated the effect of the ESLs using spiro and gold only. The perovskite-free devices were investigated in reverse bias to understand whether the ESLs suffer from pinholes. Our results, summarized in Supplementary Figure S10, show improved blocking properties for the ALD layers of both TiO₂ and SnO₂ when compared to spray pyrolysed TiO₂. This difference likely explains the cause of increased photocurrent of the latter, which, we see in Supplementary Figure S9.

A similar trend was found for planar devices using MAPbI₃ (Supplementary Figure S11). Here, the current densities measured are slightly higher in the backward but lower in the forward scan, suggesting the same limitation for charge extraction as noted above. This also matches our UPS results in Figure 1b, where the conduction bands of perovskite and TiO₂ are misaligned and highlights the importance of correct band alignment in all planar perovskite devices. Other works^{3, 19} have shown high performance at stabilized currents in thin mesoporous TiO₂ based ESLs, and we note that this may be due to a proper band alignment intrinsic to the mesoporous TiO₂/Perovskite interface which is different from the planar configuration with the TiO₂ used in this study.

We hypothesize that the preconditioning under forward bias leads to accumulation of negative charge and ion migration at the ESL-perovskite interface inducing a high electric field and/or dipole formation at this interface.^{10, 22} An elevated electric field or possibly a reduced conduction band offset can facilitate electron injection into the ESL. After releasing the positive bias, this beneficial effect lasts for a few seconds only, which is the time needed for this charge to be removed. Sweep rates in this time range give rise to large hysteresis. For the SnO₂ devices, the energy levels are already well aligned without biasing the device. Thus, charge collection is efficient showing high FF and J_{sc} independent of the scan rate (Figure 4c).

Conclusions

In summary, we have demonstrated that a barrier-free band alignment between the perovskite light harvester and the charge selective contact is of great importance for an efficient PSC. We found that planar PSCs employing the compact and pinhole-free semi-

crystalline TiO₂ layer made by ALD exhibit a band misalignment, leading to strong hysteresis behavior and scan rate dependent current densities, indicating capacitive effects at the interface. We chose a layer of SnO₂, due to its deeper conduction band, as the electron selective contact, which achieved voltages and PCEs exceeding 1.19 V and 18%, respectively. We proved that modifying the conduction band of the ESL can result in planar, high performance PSCs with high voltages and remarkably good stability over time. Furthermore, femtosecond TA measurements clearly show that the mixed (FAPbI₃)_{0.85}(MAPbBr₃)_{0.15} perovskite materials extract charges efficiently into SnO₂ but not into TiO₂ corroborating the band misalignment at the TiO₂/perovskite interface. From this we can conclude that a barrier-free charge transport across the SnO₂/perovskite interface gives rise to the high and stable current densities – regardless of sweep rate – which are not observed in TiO₂ based devices. This study highlights the importance of a perfect band alignment for highly efficient PSCs, especially in planar devices with compact charge selective layers.

Methods

Electron selective layer preparation

F:SnO₂ substrates were first wiped with acetone, and then cleaned for 10 min in piranha solution (H₂SO₄/H₂O₂ = 3:1) followed by 10 min in a plasma cleaner prior to ALD deposition.

Atomic layer deposition (ALD) of semi-crystalline TiO₂³⁴ was carried out in a Savannah ALD 100 instrument (Cambridge Nanotech Inc.) at 120 °C using tetrakis(dimethylamino)titanium(IV) (TDMAT, 99.999% pure, Sigma Aldrich) and H₂O₂. TDMAT was held at 75 °C and H₂O₂ at room temperature. The growth rate was 0.07 nm/cycle at a N₂ flow rate of 5 sccm as measured by ellipsometry.

SnO₂ was deposited at 118 °C using Tetrakis(dimethylamino)tin(IV) (TDMASn, 99.99%-Sn, Strem Chemicals INC) and ozone at a constant growth rate of 0.065 nm/cycle measured by ellipsometry. TDMASn was held at 65 °C. Ozone was produced by an ozone generator ((AC-2025, IN USA Incorporated) fed with oxygen gas (99.9995% pure, Carbagas) producing a concentration of 13% ozone in O₂. Nitrogen was used as a carrier gas (99.9999% pure, Carbagas) with a flow rate of 10 sccm.

Nb₂O₅ was deposited at 170 °C and a carrier gas flow rate of 20 sccm using (tert-butylimido)bis(diethylamino)Niobium (TBTDEN, Digital Specialty Chemicals, Canada) and ozone with a constant growth rate of 0.06 nm/cycle. TBTDEN was held at 130 °C.

Perovskite precursor solution and film preparation

Before perovskite deposition, the ALD layers were treated with UV ozone for 10 min to remove by-products from the deposition process. The perovskite films were deposited

from a precursor solution containing FAI (1 M), PbI_2 (1.1 M, TCI Chemicals), MABr (0.2 M) and PbBr_2 (0.2 M, AlfaAesar) in anhydrous DMF:DMSO 4:1 (v:v, Acros). The perovskite solution was spin-coated in a two-step program; first at 1000 for 10 s and then at 4000 rpm for 30 s. During the second step, 100 μL of chlorobenzene were poured on the spinning substrate 15 s prior the end of the program. The substrates were then annealed at 100 $^\circ\text{C}$ for 1 h in a nitrogen filled glove box.

The spiro-OMeTAD (Merck) solution (70 mM in chlorobenzene) was spun at 4000 rpm for 20 s. The spiro-OMeTAD was doped at a molar ratio of 0.5, 0.03 and 3.3 with bis(trifluoromethylsulfonyl)imide lithium salt (Li-TFSI, Sigma Aldrich), tris(2-(1H-pyrazol-1-yl)-4-tert-butylpyridine)-cobalt(III) tris(bis(trifluoromethylsulfonyl)imide) (FK209, Dyenamo) and 4-tert-Butylpyridine (TBP, Sigma Aldrich), respectively.^{22, 35, 36}

As a last step 70-80 nm of gold top electrode were thermally evaporated under high vacuum.

Solar cell characterization

A ZEISS Merlin HR-SEM was used to characterize the morphology of the device cross-section. The solar cells were measured using a 450 W xenon light source (Oriel). The spectral mismatch between AM 1.5G and the simulated illumination was reduced by the use of a Schott K113 Tempax filter (Präzisions Glas & Optik GmbH). The light intensity was calibrated with a Si photodiode equipped with an IR-cutoff filter (KG3, Schott) and it was recorded during each measurement. Current-voltage characteristics of the cells were obtained by applying an external voltage bias while measuring the current response with a digital source meter (Keithley 2400). The voltage scan rate was 10 mV s^{-1} and no device preconditioning was applied before starting the measurement, such as light soaking or forward voltage bias applied for long time. The starting voltage was

determined as the potential at which the cells furnished 1 mA in forward bias, no equilibration time was used. The cells were masked with a black metal mask limiting the active area to 0.16 cm² and reducing the influence of the scattered light. It is important to note that the devices achieved the highest hysteresis-free efficiency after 1 week of preparation.

The EQE spectra were measured under constant white light bias with an intensity of 10 mW cm⁻² supplied by a LED array. The superimposed monochromatic light was chopped at 2 Hz. The homemade system comprises a 300 W Xenon lamp (ICL Technology), a Gemini-180 double-monochromator with 1200 grooves/mm grating (Jobin Yvon Ltd) and a lock-in amplifier (SR830 DSP, Stanford Research System). The EQE integration was performed according to the following equation

$$J_{sc} = \int_{\lambda_1}^{\lambda_2} q \cdot \phi \cdot EQE \, d\lambda$$

with λ being the wavelength, q the elementary charge and ϕ the photon flux calculated from the ratio of the AM1.5 G spectral irradiance and the photon energy.

Acknowledgements

UPS and XPS were performed at the Advanced Research Division, Panasonic Corporation in Japan. HR-SEM images were taken at the Centre for Electron Microscopy (CIME) at EPFL. L.S. acknowledges support from the European FP7 FET project PHOCS (no. 309223). A.A. has received funding from the European Union's Seventh Framework Programme for research, technological development and demonstration under grant agreement no 291771. W.T., M.S. and M.K.N. thank the European Union for funding within the Seventh Framework Program (FP7/2007-2013) under grant agreement n° 604032 of the MESO project.

Author contributions

J.P.C.B. developed the basic concept and coordinated the project. ALD layers were prepared by J.P.C.B. and L.S. Devices were prepared by J.P.C.B., A.A., M.S., T.M. and F.G. Measurements were performed by J.P.C.B., L.S., W.T., A.A., M.S., T.M., F.G., S.N. and A.R.S.K. A.P supervised the femtosecond spectroscopy measurements. S.M.Z., A.A., M.K.N and M.G. contributed with fruitful discussions. A.H. supervised the project. All authors contributed to the writing of the paper.

Additional information

Supplementary information is available in the online version of the paper. Reprints and permissions information is available online at www.nature.com/reprints. Correspondence and requests for materials should be addressed to A.H. or J.P.C.B.

Competing financial interests

The authors declare no competing financial interests.

References

1. C. R. Kagan, D. B. Mitzi and C. D. Dimitrakopoulos, *Science*, 1999, **286**, 945-947.
2. A. Kojima, K. Teshima, Y. Shirai and T. Miyasaka, *Journal of the American Chemical Society*, 2009, **131**, 6050-6051.
3. W. S. Yang, J. H. Noh, N. J. Jeon, Y. C. Kim, S. Ryu, J. Seo and S. I. Seok, *Science*, 2015.
4. M. M. Lee, J. Teuscher, T. Miyasaka, T. N. Murakami and H. J. Snaith, *Science*, 2012, **338**, 643-647.
5. L. Etgar, P. Gao, Z. Xue, Q. Peng, A. K. Chandiran, B. Liu, M. K. Nazeeruddin and M. Grätzel, *Journal of the American Chemical Society*, 2012, **134**, 17396-17399.
6. S. D. Stranks, G. E. Eperon, G. Grancini, C. Menelaou, M. J. Alcocer, T. Leijtens, L. M. Herz, A. Petrozza and H. J. Snaith, *Science*, 2013, **342**, 341-344.
7. M. Liu, M. B. Johnston and H. J. Snaith, *Nature*, 2013, **501**, 395-398.
8. K. Wojciechowski, S. D. Stranks, A. Abate, G. Sadoughi, A. Sadhanala, N. Kopidakis, G. Rumbles, C.-Z. Li, R. H. Friend and A. K.-Y. Jen, *ACS nano*, 2014, **8**, 12701-12709.
9. K. Wojciechowski, T. Leijtens, S. Spirova, C. Schlueter, M. Hoerantner, J. T.-W. Wang, C.-Z. Li, A. K. Y. Jen, T.-L. Lee and H. J. Snaith, *The Journal of Physical Chemistry Letters*, 2015.
10. Y. Zhang, M. Liu, G. E. Eperon, T. C. Leijtens, D. McMeekin, M. Saliba, W. Zhang, M. de Bastiani, A. Petrozza, L. M. Herz, M. B. Johnston, H. Lin and H. J. Snaith, *Materials Horizons*, 2015, **2**, 315-322.
11. W. Ke, G. Fang, Q. Liu, L. Xiong, P. Qin, H. Tao, J. Wang, H. Lei, B. Li, J. Wan, G. Yang and Y. Yan, *Journal of the American Chemical Society*, 2015, **137**, 6730-6733.
12. Q. Dong, Y. Shi, K. Wang, Y. Li, S. Wang, H. Zhang, Y. Xing, Y. Du, X. Bai and T. Ma, *The Journal of Physical Chemistry C*, 2015, **119**, 10212-10217.
13. J. Song, E. Zheng, J. Bian, X.-F. Wang, W. Tian, Y. Sanehira and T. Miyasaka, *Journal of Materials Chemistry A*, 2015, **3**, 10837-10844.
14. Y. Li, J. Zhu, Y. Huang, F. Liu, M. Lv, S. Chen, L. Hu, J. Tang, J. Yao and S. Dai, *RSC Advances*, 2015, **5**, 28424-28429.
15. L. Kranz, A. Abate, T. Feurer, F. Fu, E. Avancini, J. Löckinger, P. Reinhard, S. M. Zakeeruddin, M. Grätzel, S. Buecheler and A. N. Tiwari, *The Journal of Physical Chemistry Letters*, 2015, 2676-2681.
16. E. M. Miller, Y. Zhao, C. C. Mercado, S. K. Saha, J. M. Luther, K. Zhu, V. Stevanovic, C. L. Perkins and J. van de Lagemaat, *Physical Chemistry Chemical Physics*, 2014, **16**, 22122-22130.
17. A. Guerrero, E. J. Juarez-Perez, J. Bisquert, I. Mora-Sero and G. Garcia-Belmonte, *Applied Physics Letters*, 2014, **105**, 133902.
18. W. Tress, N. Marinova, T. Moehl, S. M. Zakeeruddin, M. K. Nazeeruddin and M. Grätzel, *Energy & Environmental Science*, 2015, **8**, 995-1004.
19. N. J. Jeon, J. H. Noh, W. S. Yang, Y. C. Kim, S. Ryu, J. Seo and S. I. Seok, *Nature*, 2015, **517**, 476-480.

20. H. Bender, W. D. Chen, J. Portillo, L. Van den Hove and W. Vandervorst, *Applied Surface Science*, 1989, **38**, 37-47.
21. G. Xing, N. Mathews, S. Sun, S. S. Lim, Y. M. Lam, M. Grätzel, S. Mhaisalkar and T. C. Sum, *Science*, 2013, **342**, 344-347.
22. H. J. Snaith, A. Abate, J. M. Ball, G. E. Eperon, T. Leijtens, N. K. Noel, S. D. Stranks, J. T.-W. Wang, K. Wojciechowski and W. Zhang, *The Journal of Physical Chemistry Letters*, 2014, **5**, 1511-1515.
23. C. Tao, S. Neutzner, L. Colella, S. Marras, A. R. Srimath Kandada, M. gandini, M. De Bastiani, G. Pace, L. Manna, M. Caironi, C. Bertarelli and a. petrozza, *Energy & Environmental Science*, 2015.
24. G. Xing, B. Wu, S. Chen, J. Chua, N. Yantara, S. Mhaisalkar, N. Mathews and T. C. Sum, *Small*, 2015.
25. J. M. Azpiroz, E. Mosconi, J. Bisquert and F. De Angelis, *Energy & Environmental Science*, 2015.
26. W. Tress, N. Marinova, O. Inganäs, M. K. Nazeeruddin, S. M. Zakeeruddin and M. Graetzel, *Advanced Energy Materials*, 2015, **5**, n/a-n/a.
27. R. Marschall, *Advanced Functional Materials*, 2014, **24**, 2421-2440.
28. P. Docampo, F. C. Hanusch, S. D. Stranks, M. Döblinger, J. M. Feckl, M. Ehrensperger, N. K. Minar, M. B. Johnston, H. J. Snaith and T. Bein, *Advanced Energy Materials*, 2014, **4**, n/a-n/a.
29. Q. Chen, H. Zhou, Z. Hong, S. Luo, H.-S. Duan, H.-H. Wang, Y. Liu, G. Li and Y. Yang, *Journal of the American Chemical Society*, 2014, **136**, 622-625.
30. J. Xu, A. Buin, A. H. Ip, W. Li, O. Voznyy, R. Comin, M. Yuan, S. Jeon, Z. Ning, J. J. McDowell, P. Kanjanaboos, J.-P. Sun, X. Lan, L. N. Quan, D. H. Kim, I. G. Hill, P. Maksymovych and E. H. Sargent, *Nat Commun*, 2015, **6**.
31. A. H. Ip, L. N. Quan, M. M. Adachi, J. J. McDowell, J. Xu, D. H. Kim and E. H. Sargent, *Applied Physics Letters*, 2015, **106**, 143902.
32. B. Wu, K. Fu, N. Yantara, G. Xing, S. Sun, T. C. Sum and N. Mathews, *Advanced Energy Materials*, 2015, n/a-n/a.
33. E. L. Unger, E. T. Hoke, C. D. Bailie, W. H. Nguyen, A. R. Bowring, T. Heumuller, M. G. Christoforo and M. D. McGehee, *Energy & Environmental Science*, 2014, **7**, 3690-3698.
34. J. Azevedo, L. Steier, P. Dias, M. Stefik, C. T. Sousa, J. P. Araujo, A. Mendes, M. Graetzel and S. D. Tilley, *Energy & Environmental Science*, 2014, **7**, 4044-4052.
35. A. Abate, T. Leijtens, S. Pathak, J. Teuscher, R. Avolio, M. E. Errico, J. Kirkpatrick, J. M. Ball, P. Docampo, I. McPherson and H. J. Snaith, *Physical Chemistry Chemical Physics*, 2013, **15**, 2572-2579.
36. A. Abate, D. R. Staff, D. J. Hollman, H. J. Snaith and A. B. Walker, *Physical Chemistry Chemical Physics*, 2014, **16**, 1132-1138.